Bifunctional TiO$_2$/COF S-scheme photocatalyst with enhanced H$_2$O$_2$ production and furoic acid synthesis mechanism

Yi Yang [a], Jingjing Liu [a], Miaoli Gu [a], Bei Cheng [a], Linxi Wang [b,*], Jiaguo Yu [b,*]

[a] *State Key Laboratory of Advanced Technology for Materials Synthesis and Processing, Wuhan University of Technology, Wuhan 430070, PR China*
[b] *Laboratory of Solar Fuel, Faculty of Materials Science and Chemistry, China University of Geosciences, 68 Jincheng Street, Wuhan 430078, China*

ARTICLE INFO

ABSTRACT

Coupling photocatalytic H$_2$O$_2$ evolution with simultaneous furfuryl alcohol oxidation can avoid the slow water oxidation reaction and fully utilize photogenerated carriers to produce valuable chemicals. Herein, a COF (denoted as BTTA) was synthesized by the Schiff-base condensation and in-situ grown on the surface of TiO$_2$ nanofibers. The resultant TiO$_2$/BTTA composite has a large interface and a short carrier migration distance. Furthermore, the porous and ultrathin BTTA layers endow the composites abundant active sites and excellent light absorption ability. Remarkably, a H$_2$O$_2$-evolution rate of 740 µmol L^{-1} h^{-1} and a furoic alcohol conversion of 96 % are achieved. In-situ irradiated X-ray photoelectron spectroscopy and electron spin resonance confirm the S-scheme carrier transfer mechanism, which spatially separates photogenerated carriers with strong redox power. This work opens a new door to the rational design of S-scheme photocatalysts for economic and green photosynthesis of H$_2$O$_2$ and organic compounds.

1. Introduction

Hydrogen peroxide (H$_2$O$_2$) is an ideal liquid energy carrier because of its high energy density and easy storage. In addition, as an environment-friendly oxidant, H$_2$O$_2$ is widely used in environmental remediation, sterilization, and chemical manufacturing [1–4]. Currently, commercial H$_2$O$_2$ production is mainly based on the anthraquinone oxidation/reduction process, which requires intensive energy input and produces hazardous waste [5,6]. An alternative to this energy-intensive process, direct synthesis from H$_2$ and O$_2$ can quantitatively produces H$_2$O$_2$, but the high cost of noble metal catalysts and the explosion risk of H$_2$/O$_2$ mixture limit its large-scale industrial applications. In comparison, photocatalytic production of H$_2$O$_2$ from earth-abundant water and O$_2$ is a promising method due to its safe, energy-saving and nonpolluting properties [7,8].

In general, photocatalytic H$_2$O$_2$ production proceeds through O$_2$ reduction by photogenerated electrons (e$^-$) via the proton-coupled two-electron process (O$_2$ + 2 H$^+$ + 2e$^-$ → H$_2$O$_2$; E° = 0.68 V$_{NHE}$, NHE stands for normal hydrogen electrode). Meanwhile, photogenerated holes (h$^+$) oxidize water to protons and O$_2$ (H$_2$O + 4 h$^+$ → 4 H$^+$ + O$_2$; E° = 1.23 V$_{NHE}$). However, the sluggish water oxidation severely decelerates the kinetics of the overall reaction. Therefore, alcohols with higher oxidability are used as electron donors to consume photogenerated holes [9,10]. Nevertheless, alcohols are valuable chemicals, and the usage of alcohols as sacrificial agents is not economically desirable. Instead, coupling photocatalytic H$_2$O$_2$ production with selective oxidation of organic compounds can not only consume the holes to produce value-added chemicals, but also replace the slow water oxidation reaction to increase H$_2$O$_2$ productivity. For example, the photocatalytic oxidation of biomass-derived furan is of great significance [11,12]. Recently, photocatalytic oxidation of furfuryl alcohol (FAL) to furoic acid (FAC) has attracted enormous interest as the concomitant reaction of H$_2$O$_2$ photosynthesis since FAC is a crucial intermediate for the manufacturing of plasticizers, thermosetting resins, preservatives, coatings additives, and medicines [13]. Therefore, developing efficient dual-functional photocatalysts for H$_2$O$_2$ evolution and selective FAL oxidation is a promising direction.

Single-component photocatalysts such as TiO$_2$ [14–16], ZnO [17], CdS [18,19], and C$_3$N$_4$ [20–23] are not ideal for photocatalytic reactions due to the tradeoff between a wide light absorption range and strong redox abilities. In addition, rapid charge carrier recombination severely limits the photocatalytic activity. Rational design of S-scheme heterojunctions is a promising solution given that it facilitates the spatial separation of photogenerated charge carriers and maximizes redox
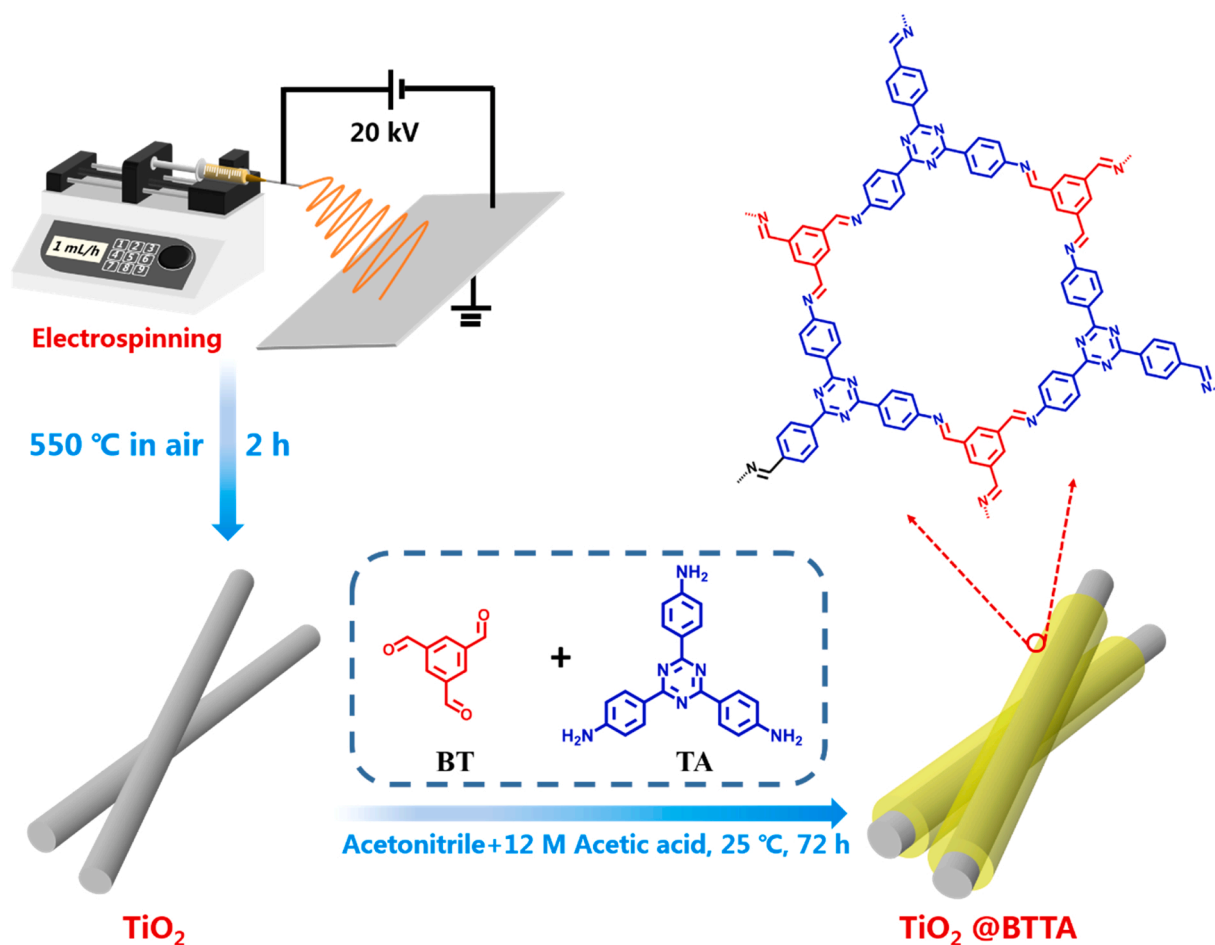
* Corresponding authors.
E-mail addresses: linxiwang91@126.com (L. Wang), yujiaguo93@cug.edu.cn (J. Yu).

Scheme 1. Synthetic procedure of TiO$_2$ @BTTA composites.

power [24,25]. Specifically, the formation of an internal electric field (IEF) within the S-scheme heterojunction boost the migration of photogenerated carriers to surface reactive sites [26–28]. The electrons and holes with strong redox abilities can simultaneously achieve O$_2$ reduction to H$_2$O$_2$ and selective FAL oxidation to FAC, respectively.

Herein, for the first time, we designed TiO$_2$ nanofibers (NFs) encapsulated by the BTTA-COF for efficient photocatalytic H$_2$O$_2$ production and selective FAL oxidation. As a representative oxidation photocatalyst, TiO$_2$ has several advantages such as high abundancy, low toxicity, and excellent chemical stability. Importantly, the oxidation potential of TiO$_2$ is positive enough to drive FAL oxidation to FAC. Porous BTTA was hybridized with TiO$_2$ owing to their large surface areas, great visible light absorbance, and strong reducing power for O$_2$-to-H$_2$O$_2$ conversion. In addition, the π-conjugated system of BTTA provides large carrier transport channels. The S-scheme TiO$_2$/BTTA heterojunction promotes the spatial separation and migration of photogenerated charge carriers and simultaneously preserves the strong redox capacity of the photocatalytic system, leading to high performance in H$_2$O$_2$ production and FAL oxidation. This work illustrates a novel design of dual-functional S-scheme photocatalysts for simultaneous H$_2$O$_2$ production and organic synthesis.

2. Experimental section

2.1. Chemicals and materials

All chemicals and solvents were of analytical grade and used without further purification. Tetrabutyl titanate (TBT), isopropanol (IPA), silver nitrate (AgNO$_3$), ethanol, acetic acid (CH$_3$COOH), acetonitrile (CH$_3$CN),

triethanolamine (TEOA), and N, N-dimethylformamide (DMF) were purchased from Sinopharm Chemical Reagent Co., Ltd. Furfuryl alcohol, poly(vinyl pyrrolidone) (PVP, MW= 1,300,000), 4,4′,4″-(1,3,5-triazine-2,4,6-triyl)trianiline (TA) and 1,3,5-benzenetricarboxaldehyde (BT) were purchased from Aladdin. Potassium iodide (KI), p-Benzoquinone (C$_6$H$_4$O$_2$) and 5,5-Dimethyl-1-pyrroline N-oxide (DMPO) were bought from Shanghai Macklin Biochemical Co., Ltd.

2.2. Preparation of TiO$_2$ NFs

TiO$_2$ NFs were synthesized via electrospinning according to our previously published work [29]. First, 2 g of TBT was dissolved in a solvent containing 10 g of ethanol and 2 g of acetic acid and stirred for 0.5 h. Subsequently, 0.75 g of PVP was added to the solution, which was further stirred for 6 h at room temperature until a polymeric sol–gel was formed. Then, the transparent pale-yellow solution was transferred to a syringe for electrospinning at an injection rate of 1 mL h^{-1}. An AC voltage of 20 kV was applied, and the distance between the plate collector and the syringe needle (21 G) was 15 cm. The resultant fibers were calcined at 550 °C for 2 h at a heating rate of 2 °C min^{-1} to obtain the TiO$_2$ NFs.

2.3. Preparation of BTTA

For BTTA preparation, 6.5 mg of BT, 14.2 mg of TA, and 5 mL of acetonitrile were added into a Pyrex tube. After 30 min of ultrasonication, 0.4 mL of acetic acid (12 M) was added to the reaction system. The tube was flash-frozen by liquid nitrogen, degassed and then filled with N$_2$ and sealed. The mixture was kept at 25 °C for 72 h without
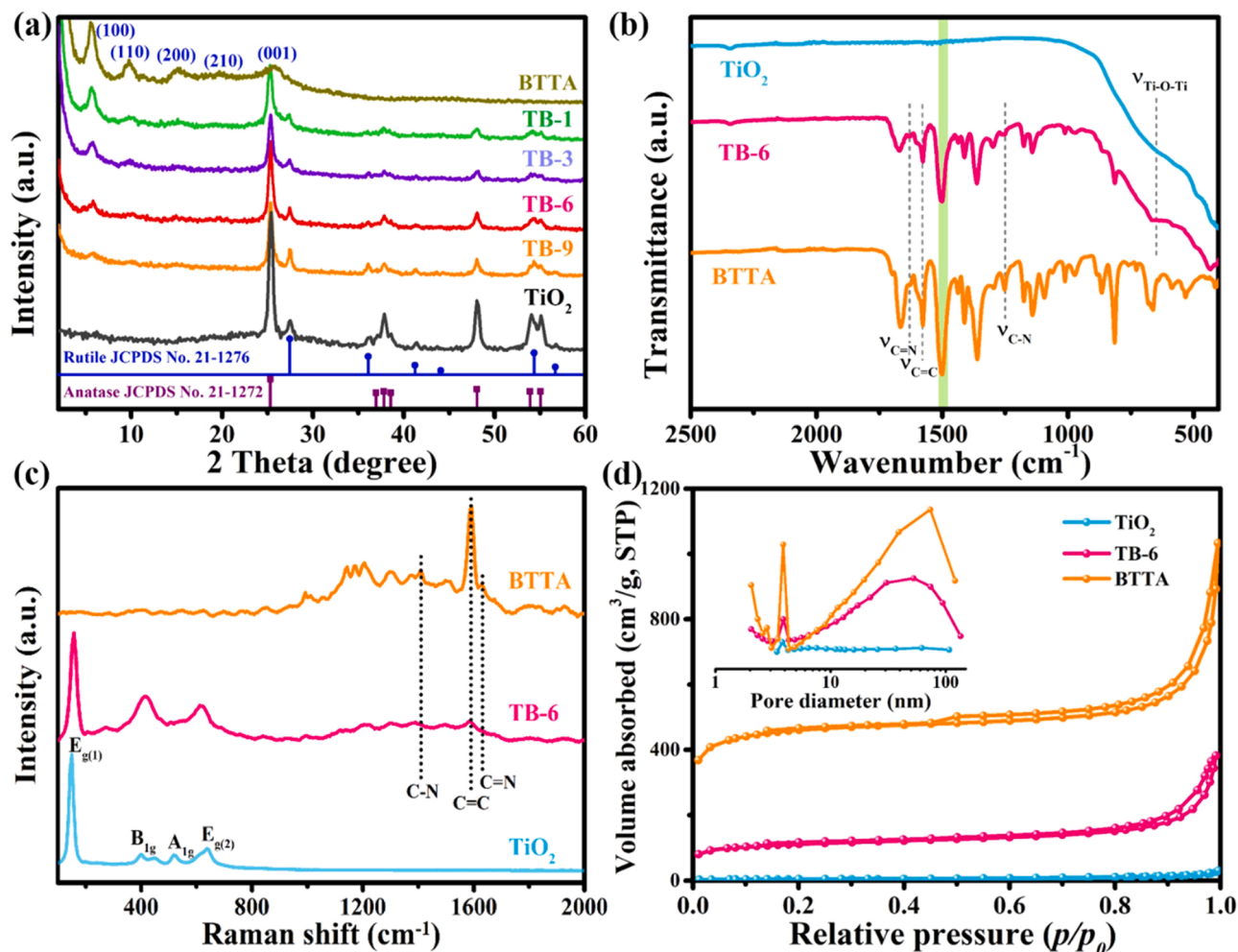
Fig. 1. (a) PXRD spectra of TiO$_2$, BTTA, and TB-X; (b) FTIR and (c) Raman spectra of TiO$_2$, BTTA, and TB-6; (d) N$_2$ physisorption isotherms and pore size distribution curves (inset) of TiO$_2$, BTTA, and TB-6.

stirring. The product was centrifuged, washed with DMF, and then dried in a vacuum oven at 80 °C for 12 h to obtain the yellow BTTA.

2.4. Preparation of TiO$_2$@BTTA nanocomposite

Typically, 14.2 mg of TA, 3 mL of acetonitrile and a certain amount of TiO$_2$ NFs were added into a Pyrex tube. After 60 min of ultra-sonication, 6.5 mg of BT and 2 mL of acetonitrile were added into the tube. After sonication for another 30 min, 0.4 mL of acetic acid (12 M) was added to trigger polymerization. The tube was sealed, filled with N$_2$, and then kept at room temperature for 72 h. The obtained yellow solids were filtered, washed with DMF, and dried in a vacuum oven at 80 °C for 12 h. By varying the amount of TiO$_2$, TiO$_2$@BTTA hybrid materials with different compositions were obtained. The composites were named as TB-X, where X is the TiO$_2$:BTTA weight ratio (TB-1 (TiO$_2$:BTTA = 1:1), TB-3 (3:1), TB-6 (6:1), and TB-9 (9:1)).

2.5. Characterization and performance measurement

Detailed information on characterization and photocatalytic performance tests is included in the supporting information.

3. Results and discussions

3.1. Structure and morphology

The synthesis of TiO$_2$@BTTA is illustrated in Scheme 1. In the first step, TiO$_2$ NFs were synthesized by electrospinning and calcination [30]. Subsequently, through Schiff-base reaction, BTTA was in-situ grown on TiO$_2$ surfaces to form TiO$_2$@BTTA hybrids with core-shell structures. The crystalline structures of TiO$_2$, BTTA, and TiO$_2$@BTTA composites were confirmed by the powder X-ray diffraction (PXRD) patterns (Fig. 1a). The five main peaks at 5.6°, 9.7°, 15.1°, 19.7°, and 25.7° correspond to the (100), (110), (200), (210), and (001) planes of crystalline BTTA. All the characteristic diffraction peaks are in good agreement with the eclipsed AA stacking mode referring to previous literature [31]. The diffraction peaks of TiO$_2$ NFs can be indexed to a mixture of anatase (JCPDS Card No. 21-1272) and rutile TiO$_2$ (JCPDS Card No. 21-1276). The PXRD patterns of all TiO$_2$@BTTA hybrids exhibit the characteristic peaks of both TiO$_2$ and BTTA. As the TiO$_2$ content decreases, the intensities of TiO$_2$-related peaks slightly weaken. For all the hybrids, the intensities of BTTA-related peaks are much lower than those of TiO$_2$-related peak. This might be attributed to its lower weight loading and poorer crystallinity than those of TiO$_2$.

In the Fourier transform infrared (FTIR) spectra of BTTA and TB-6 (Fig. 1b), the peaks at 1629 cm^{-1} (C═N), 1580 cm^{-1} (C═C), and 1245 cm^{-1} (C–N) correspond to the imine units in BTTA frameworks [32,33]. The strong peak at 1510 cm^{-1} is ascribed to the semicircle
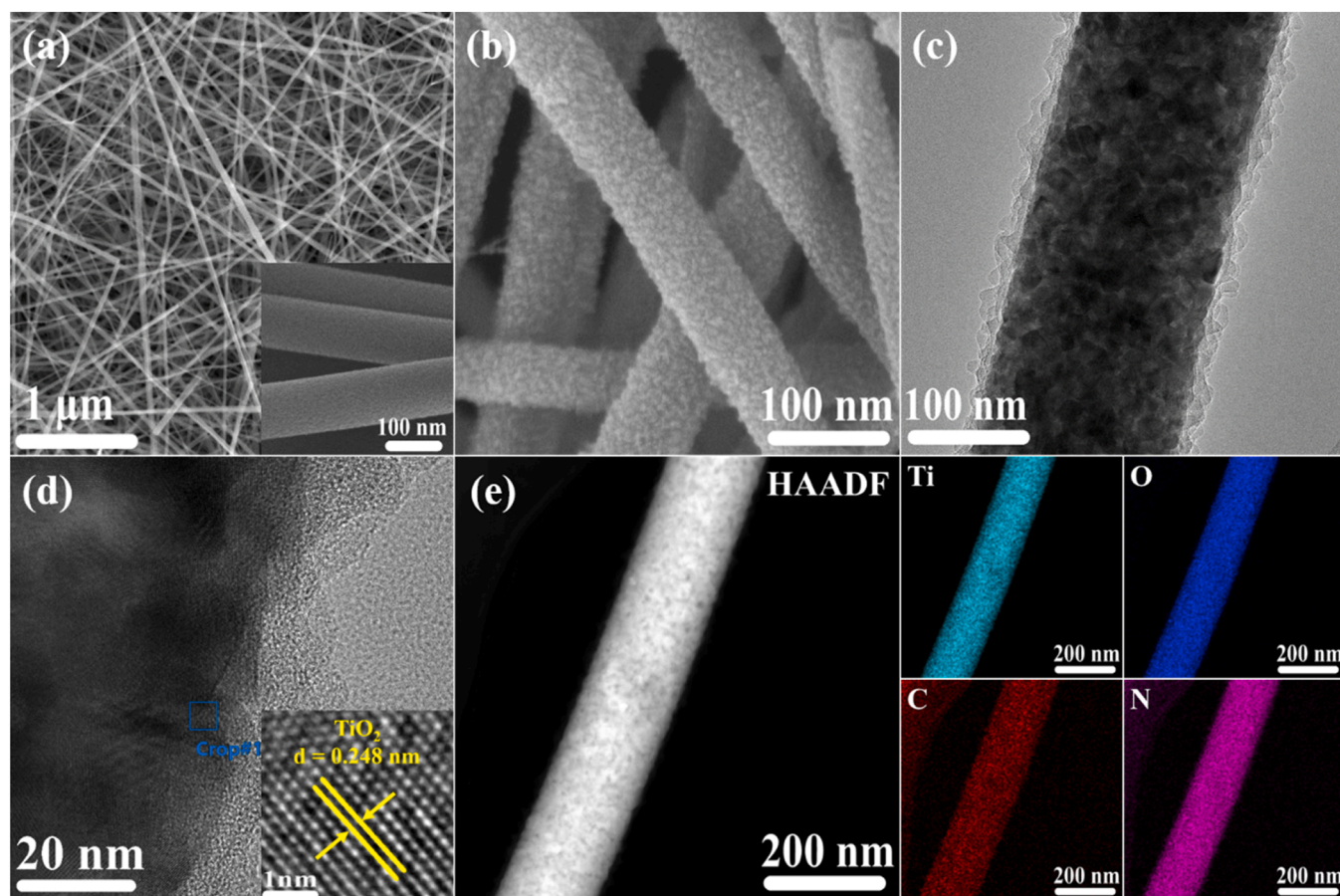
Fig. 2. FESEM image of (a) TiO$_2$ and (b) TB-6; (c) TEM and (d) HRTEM images of TB-6; (e) STEM image of TB-6 and the corresponding EDX elemental maps.

stretching of triazine rings. For both samples, the characteristic N $-$ H stretching peaks of TA monomers (3200–3400 cm^{-1}) are not detected, and the strong C$=$O stretching peak in BT monomers at 1697 cm^{-1} was significantly weakened (Fig. S1a) [34,35]. These phenomena illustrate the thorough reaction between TA and BT monomers [36]. Moreover, the TB-6 and TiO$_2$ spectra show a broad peak at 400–750 cm^{-1}, corresponds to the characteristic vibration of Ti–O–Ti [37].

Raman spectroscopy was also conducted to confirm the structure of TiO$_2$, BTTA, and TB-6. As depicted in Fig. 1c, TB-6 and BTTA exhibit four major Raman bands at 147, 398, 518, and 639 cm^{-1}, assigned to E$_{g(1)}$, B, A$_{1\,g}$, and E$_{g(2)}$ modes of anatase TiO$_2$, respectively [38]. The E$_g$ and B$_{1\,g}$ peaks are mainly caused by the symmetric stretching and bending of O$-$Ti$-$O, respectively, while the A$_{1\,g}$ peak is caused by asymmetric bending of O$-$Ti$-$O. The characteristic peaks of BTTA at 1012 and 1590 cm^{-1} can be ascribed to the stretching vibration of benzene rings and C$=$C bonds, respectively. The peaks at 1638 and 1409 cm^{-1} belong to the symmetric stretching of C$=$N and the stretching vibration of the C–N bond, respectively [39]. Obviously, the TB-6 spectrum shows the characteristic peaks of both TiO$_2$ and BTTA, indicating the successful integration of BTTA and TiO$_2$.

The surface areas and porosities of TiO$_2$, BTTA, and TB-6 were investigated by N$_2$ physisorption measurements at 77 K, and the results are summarized in Table S1. All samples show type IV isotherms with type H3 hysteresis loops, signifying the presence of mesopores (Fig. 1d). The Brunauer–Emmett–Teller surface area (S$_{BET}$) of TB-6 (384 m^2 g^{-1}) is smaller than that of pure BTTA (1561 m^2 g^{-1}) due to the low S$_{BET}$ of TiO$_2$ NFs (14 m^2 g^{-1}). Moreover, pore size distributions were obtained using non-local density functional theory models. Two types of pores with diameters of 2.9 and 70 nm are observed for TB-6. The smaller pores were consistent with the microporous structures of imine-linked

BTTA frameworks [40]. The larger pores, which also exist in pure BTTA, are possibly derived from the aggregation of BTTA nanoparticles (Fig. S1b). This result indicates that the in-situ growth of BTTA on TiO$_2$ NFs forms a porous shell, enables access of reactants to active sites on the TiO$_2$ core.

The morphology and structure of the samples were unveiled by scanning electron microscopy (SEM) and transmission electron microscopy (TEM). As shown in Fig. 2a, TiO$_2$ NFs with an average diameter of ~100 nm are densely interlaced. The field emission SEM (FESEM) image of TB-6 (Fig. 2b) shows a rough surface caused by the deposition of BTTA layers, which are ~20 nm thick (Fig. 2c). The high-resolution TEM (HRTEM) image in Fig. 2d exhibits a lattice spacing of 0.248 nm for TiO$_2$ NFs, ascribed to the (101) crystal plane of rutile TiO$_2$. The energy-dispersive X-ray (EDX) spectra of TB-6 (Fig. 2e) discloses the even distribution of C, N, O, and Ti elements. Thermogravimetric analysis of TB-6 indicates that the weight ratio of BTTA is 12.1 %, comparable to the nominal value. Besides, all the TB-X samples show high thermal stability, since the weight loss is less than 10 % up to 350 °C (Fig. S1c).

3.2. Band diagram and XPS analysis

To analyze the band structure of TiO$_2$ @BTTA composites, the band diagrams of TiO$_2$ and BTTA are determined by optical and electrochemical measurements. First, the light adsorption properties of the samples were measured by ultraviolet−visible (UV−vis) diffuse reflectance spectroscopy (DRS). The absorption intensity of TB-6 is much stronger than that of TiO$_2$, and its absorption edge is slightly red-shifted (Fig. 3a), indicating that the unique π-conjugated structures of BTTA is beneficial for light harvesting. According to the Kubelka-Munk function equation ($\alpha h v = A (h v - E_g)^{1/2}$), the band gaps (E$_g$) of TiO$_2$ and BTTA
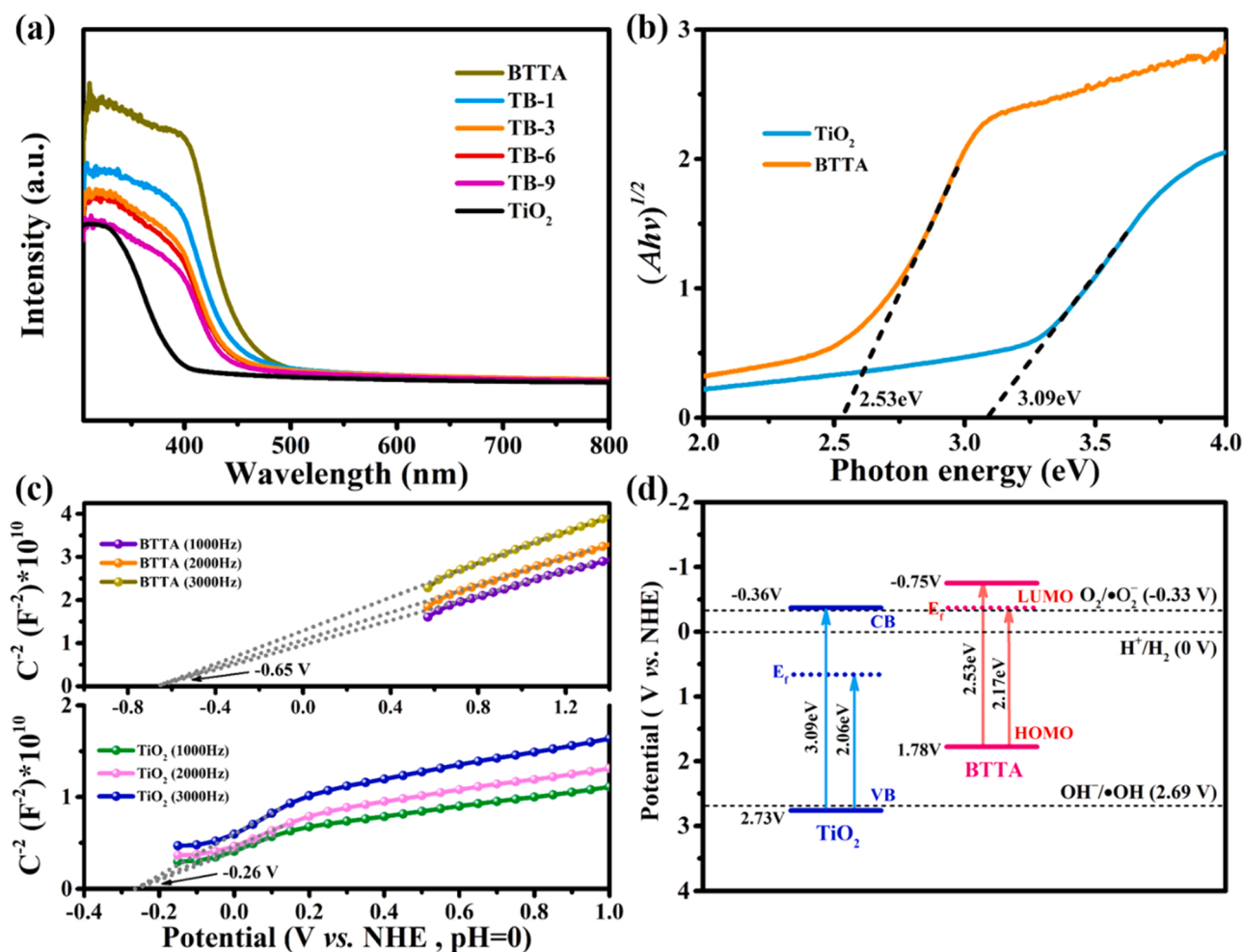
Fig. 3. (a) UV–vis DRS spectra of different photocatalysts; (b) band gaps and (c) Mott-Schottky plots of TiO_2 and BTTA; (d) Band diagrams of TiO_2@BTTA.

are 3.09 and 2.53 eV, respectively (Fig. 3b). Mott−Schottky (MS) experiments are performed to determine the band positions of TiO_2 and BTTA [41]. The MS plots of both samples present positive slopes (Fig. 3c), indicating that they are both n-type semiconductors. The flat band potentials of TiO_2 and BTTA are estimated to be − 0.26 and − 0.65 V vs NHE, respectively. Since the CB position of an n-type semiconductor is often 0.1 V higher than its flat band potential, the CB potential of TiO_2 and the lowest unoccupied molecular orbital (LUMO) level of BTTA are estimated to be − 0.36 and − 0.75 V vs NHE, respectively. Based on the bandgap values, the VB position of TiO_2 and the highest occupied molecular orbital (HOMO) of BTTA are 2.73 and 1.78 V vs NHE, respectively. Hence, TiO_2@BTTA shows a staggered band diagram (Fig. 3d), which is necessary for the construction of an S-scheme heterojunction.

In order to confirm the chemical composition of TB-6 and electron transfer at TiO_2/BTTA interfaces, in-situ irradiated X-ray photoelectron spectroscopy (ISI-XPS) measurements were conducted [42–45]. The XPS survey spectrum (Fig. S2a) of TB-6 confirms the co-existence of Ti, O, C, and N, consistent with the EDX elemental mapping results. For BTTA, the C 1 s signal is deconvoluted into three peaks with binding energies (BEs) of 284.8, 285.97, and 287.93 eV (Fig. 4a), belonging to the C−C/C=C, C−N, and C=O bonds, respectively. The N 1 s spectrum of BTTA (Fig. 4b) shows two distinct peaks at 398.65 and 400.31 eV, which are assigned to N in the pyridinic (C=N) and amino (C−N) groups of BTTA, respectively. For TiO_2, Ti 2p1/2 (464.49 eV) and Ti 2p3/2 (458.75 eV) peaks are observed in the Ti 2p spectrum (Fig. 4c), and the peaks at 530.59 and 532.28 eV in the O 1 s spectrum (Fig. 4d)

correspond to the oxygen in Ti−O and hydroxyl groups, respectively. As for TB-6, the negative shifts in the BEs of Ti 2p and O 1 s peaks suggest an increasing electron density of the TiO_2 component. In contrast, the C 1 s and N 1 s peaks of TB-6 shift to high BEs, suggesting a lower electron density in the BTTA component. These shifts indicate a strong interfacial interaction between TiO_2 and BTTA upon hybridization, where the free electrons migrate from BTTA to TiO_2. Importantly, when TB-6 is illuminated, the BEs of Ti 2p and O 1 s peaks increase, while those of C 1 s and N 1 s peaks decrease. These results clearly suggest that photogenerated electrons are transferred from TiO_2 to BTTA, revealing an S-scheme mechanism.

The VB XPS measures the energy gaps between Fermi levels (E_f) and VBs, which are 2.06 eV for TiO_2 and 2.17 eV for BTTA (Fig. S2b). Thus, the E_f of TiO_2 (0.67 V vs NHE) is lower than that of the BTTA (−0.39 V vs NHE), indicating that free electrons in BTTA would spontaneously transfer to the TiO_2 upon contact (Fig. 4e). Therefore, TiO_2 and BTTA are negatively and positively charged at the interface, respectively, resulting in the formation of an IEF. The interfacial electron transfer is in accord with the BE drifts of the XPS peaks. Under illumination, electron–hole pairs are photogenerated in both TiO_2 and BTTA. Under the action of IEF, photogenerated electrons in the CB of TiO_2 will rapidly recombine with the holes in the HOMO of BTTA. These electrons and holes with low redox abilities are eliminated, while those with high redox abilities (i.e., electrons in the VB of TiO_2 and holes in the LUMO of BTTA) are retained [46–48]. Thus, the interaction between TiO_2 and BTTA forms the S-scheme heterojunction, leading to enhanced carrier separation in space as well as boosted redox power.

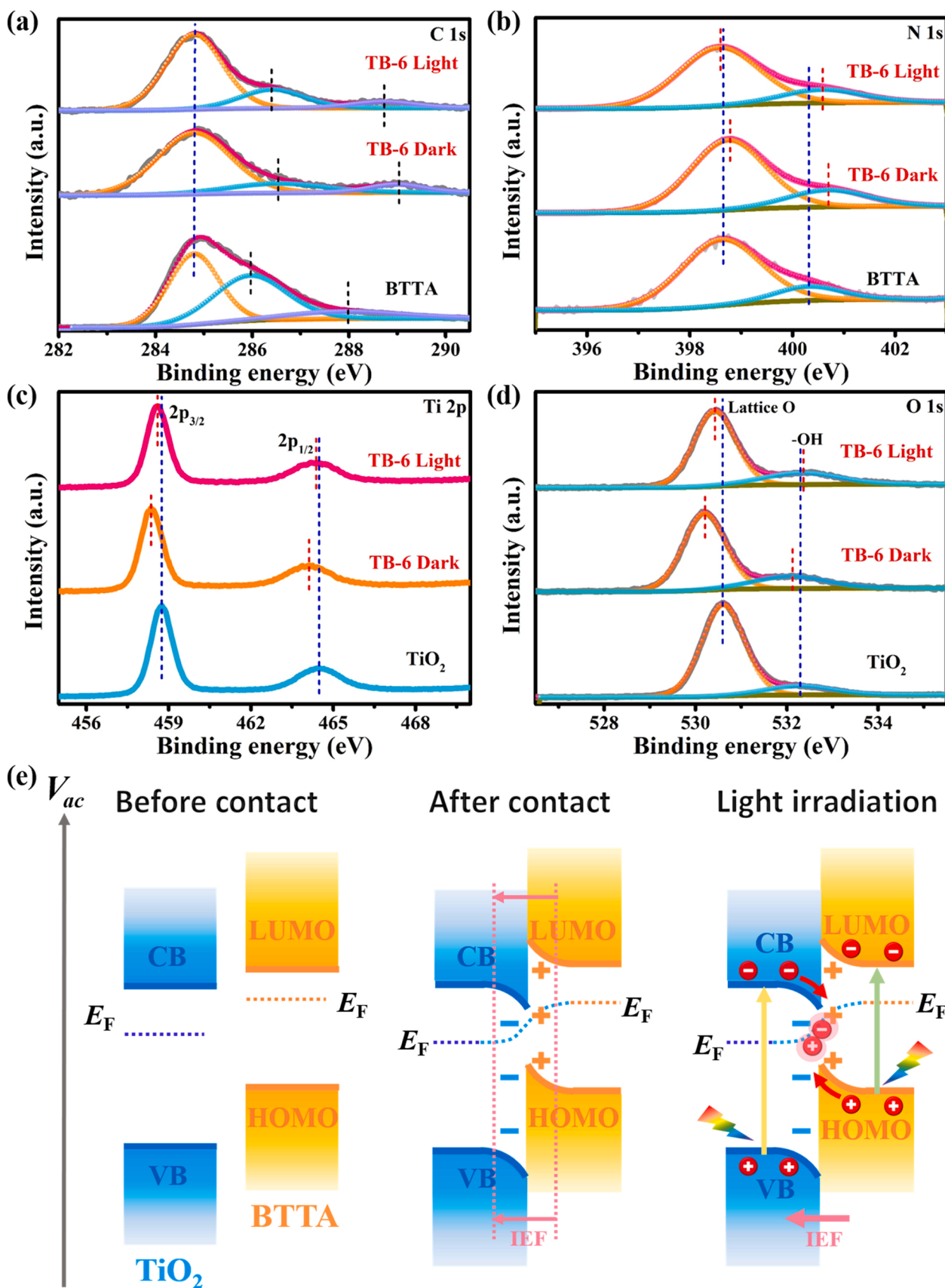**Fig. 4.** ISI-XPS spectra of (a) C 1 s, (b) N 1 s, (c) Ti 2p, and (d) O 1 s states for TiO_2, BTTA, and TB-6 in dark and under 365 nm LED illumination. (e) Charge carrier transfer mechanism of S-scheme TiO_2 @BTTA photocatalysts.
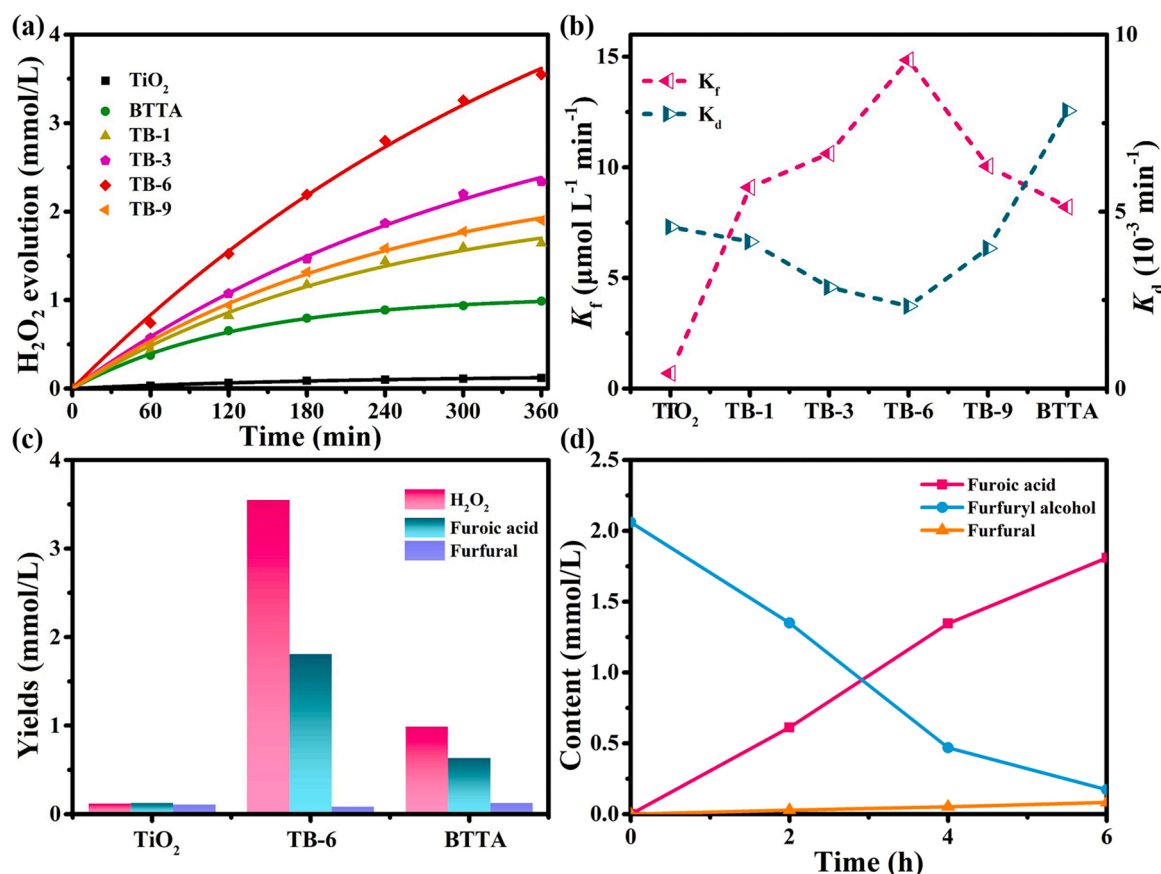
Fig. 5. (a) Photocatalytic H_2O_2 evolution yields; (b) Formation rate constant (K_f) and decomposition rate constant (K_d) for photocatalytic H_2O_2 production; (c) Yields of H_2O_2, furoic acid, and furfural over TiO_2, BTTA, and TB-6 in 6 h; (d) Time course of FAL, FF, and FAC concentrations during photocatalytic FAL oxidation over TB-6.

3.3. Photocatalytic H_2O_2 production performance

To make full use of photogenerated charge carriers, photocatalytic reactions were conducted in O_2-saturated solutions with FAL addition. In this scenario, the photogenerated electrons are used to reduce O_2 to H_2O_2, while the holes oxidize FAL to furfural (FF) and FAC. The H_2O_2 concentration was quantified by spectrophotometry with triiodide anions. The calibration curve (Fig. S3) shows a good linearity between the absorbance and H_2O_2 concentration. Fig. 5a presents the photocatalytic H_2O_2 yields over TiO_2, BTTA, and TB-X samples. TiO_2 exhibits the poorest performance with a H_2O_2 yield of 31.3 µmol L^{-1} h^{-1}, due to the rapid recombination of photogenerated carriers. After forming the TB-X composites, the H_2O_2 yield is significantly improved. Especially, TB-6 shows the highest H_2O_2 evolution rate (740 µmol L^{-1} h^{-1}), which is about 24 times higher than that of pure TiO_2 and outperforms those of many reported TiO_2-based photocatalysts (Table S2). The calculated apparent quantum yield (AQY) of TB-6 reaches 5.48 %. Generally, photocatalytic H_2O_2 production is a dynamic process including H_2O_2 formation and decomposition, the rates of which can be fitted by zero-order and first-order kinetics, respectively.

$$[H_2O_2] = K_f/K_d \times \{1 - \exp(-K_d t)\} \tag{1}$$

The rate constants of H_2O_2 formation (K_f, µM min^{-1}) and decomposition (K_d, min^{-1}) are obtained by fitting the time course of H_2O_2 yields with Eq. 1. As shown in Fig. 5b, the K_f is 14.8 µM/min for TB-6, approximately 22 times higher than that for TiO_2 (0.69 µM/min). At the same time, TB-6 displays the lowest K_d, leading to the highest overall H_2O_2 production rate.

Photocatalytic H_2O_2 production is accompanied with FAL oxidation. Fig. 5c shows the H_2O_2, FF, and FAC yields over TiO_2, BTTA, and TB-6

after 6 h of light irradiation. TB-6 shows the highest FAL conversion (92 %), approximately 15 times higher than that of TiO_2. TB-6 also exhibits high FAC selectivity (96 %) (Fig. 5d and Table S3). The products of FAL oxidation were identified and quantitatively analyzed by high-performance liquid chromatography (HPLC). As shown in Fig. S4a–d, FAL is mainly oxidized to FAC on TB-6, which is further verified by gas chromatograph–mass spectrometry (GC–MS) results (Fig. S5a-c) and ^1H nuclear magnetic resonance (NMR) spectrum (Fig. S5d). To assess the stability of TB-6, cycling experiments were performed. As shown in Figs. S6a and 6b, no significant deactivation is observed after four cycles. In addition, the morphology (Fig. S6c), crystal structure (Fig. S6d), and chemical environments of TB-6 (Fig. S7) show little change after photocatalytic reactions, manifesting its good stability.

3.4. Charge separation and transfer

The separation and transfer efficiency of photogenerated carriers is the key factor to determine photocatalytic activity. As shown in Fig. 6a, the photocurrent density of TB-6 is almost 5 times higher than that of TiO_2, reflecting enhanced light harvesting and charge carrier separation efficiency of the S-scheme heterojunction in TB-6. In addition, electro-chemical impedance spectroscopy (EIS) measurements were applied to investigate the carrier transport resistance. In the Nyquist plot (Fig. 6b), TB-6 shows the smallest semicircle, indicating that the S-scheme heterojunction effectively lowers electron transfer resistance. Steady-state photoluminescence (PL) spectra in Fig. 6c reveal a weaker fluorescence intensity of TB-6 than those of TiO_2 and BTTA, implying the lowest electron−hole recombination rate. Moreover, time-resolved PL (TRPL) spectra in Fig. 6d provide information about the lifetimes of photogenerated charge carriers. After fitting the TRPL curves with a tri-
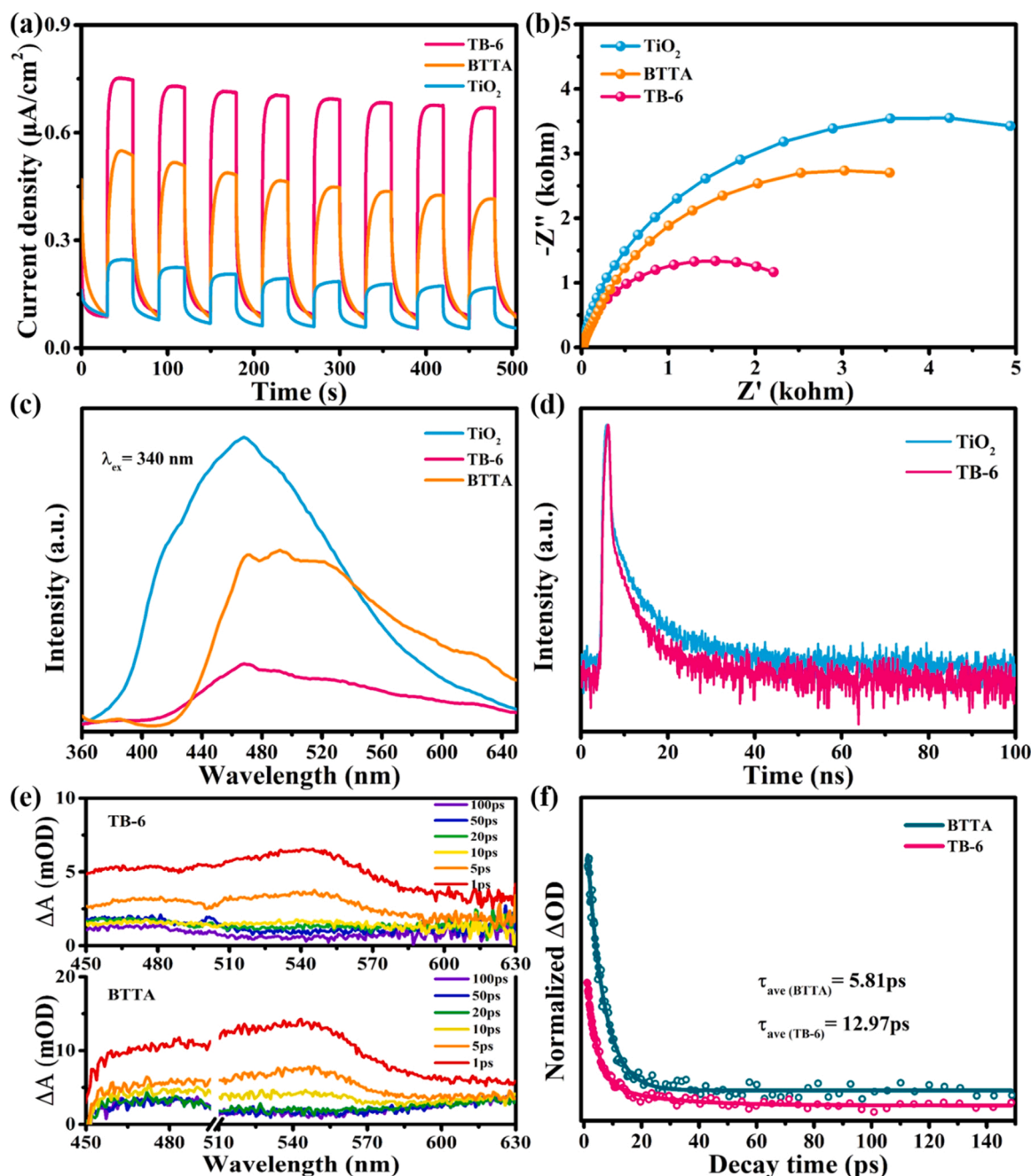
Fig. 6. (a) Transient photocurrent responses, (b) EIS spectra, (c) PL spectra, and (d) TRPL spectra of the samples; (e) fs-TA spectra of BTTA and TB-6 under 340 nm laser excitation; (f) Normalized fs-TA decay curves of BTTA and TB-6 probed at 550 nm.

exponential equation, the average carrier lifetimes for TiO_2 and TB-6 are 4.32 and 3.37 ns, respectively (Table S4). The average carrier lifetime of TB-6 is shorter than that of TiO_2, which can be interpreted as the S-scheme heterojunction prompts photogenerated carrier transfer from TiO_2 CB to BTTA HOMO, leading to the fast recombination of useless carriers. Meanwhile, the useful electrons in BTTA LUMO and holes in TiO_2 VB are preserved.

To further investigate the mechanism of photogenerated carrier transfer in the S-scheme heterojunction, femtosecond transient absorption (fs-TA) spectra on BTTA and TB-6 were collected at different time delays. As depicted in Fig. 6e, both BTTA and TB-6 show a broad positive absorption peak from 450 to 600 nm, attributed to the excited-state absorption (ESA) of trapped and free electrons in BTTA, respectively. For both samples, the ΔA signals maximize immediately after laser flash

($<$1 ps) and then gradually decay. The decay curves at 550 nm, which correspond to ESA signals, are displayed in Fig. 6f and fitted by a bi-exponential equation. TB-6 signal shows a longer average lifetime than BTTA, indicating efficient spatial carrier transfer and separation and inhibited electron–hole recombination in the S-scheme hetero-junction [49,50]. Therefore, the photogenerated electrons in BTTA and the holes in TiO_2 have sufficient time to migrate to photocatalyst surfaces and participate in catalytic redox reaction. All these results demonstrate that the S-scheme heterojunction improves carrier separation and transfer, thus improving the photocatalytic activity.

3.5. Mechanism analysis

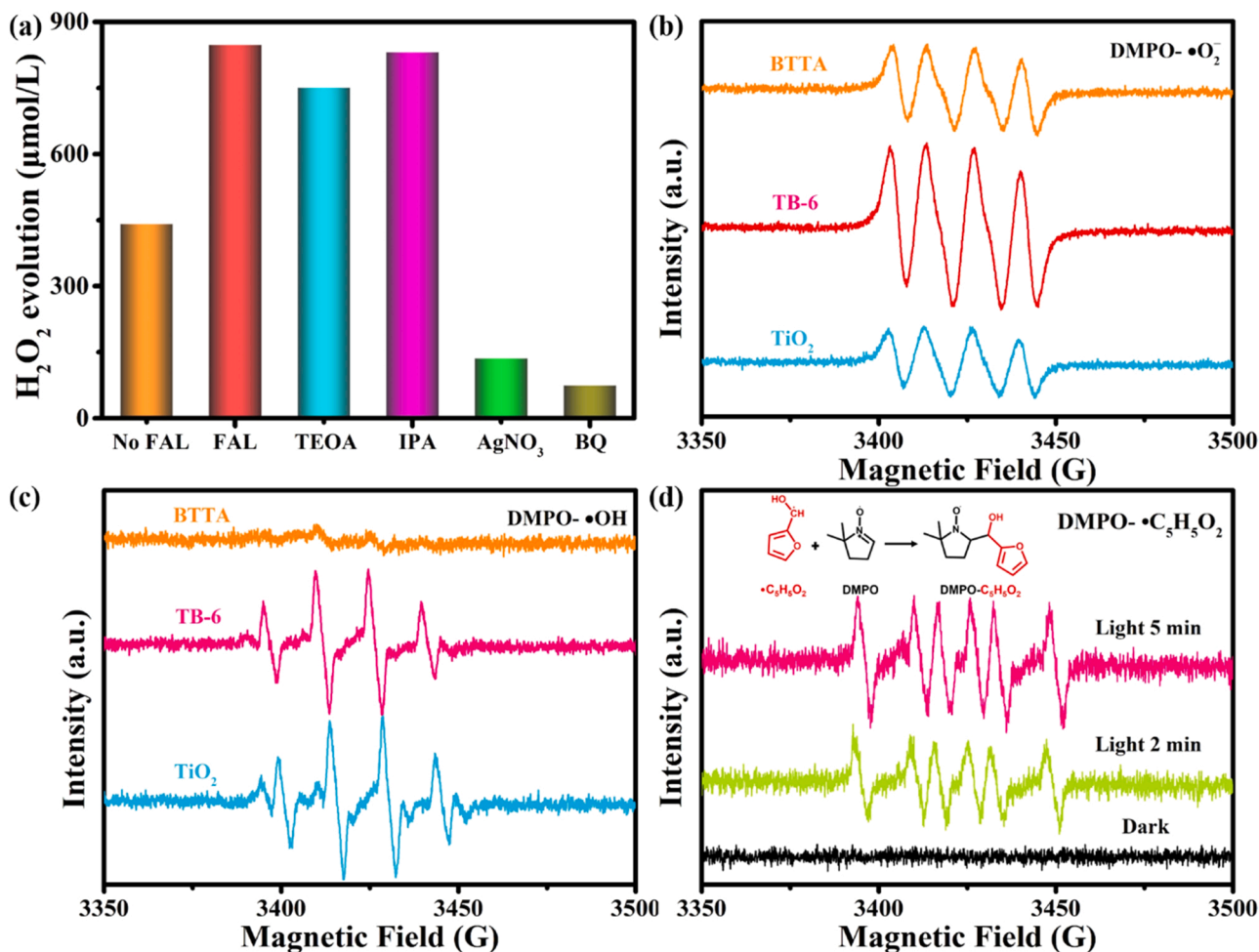To understand the pathway of H_2O_2 formation, a series of control

Fig. 7. (a) Active species trapping experiments for TB-6; (b) EPR signals of DMPO-•O_2^- on TiO$_2$, BTTA, and TB-6 in O_2-saturated methanol; (c) EPR signals of DMPO-•OH on TiO$_2$, BTTA, and TB-6 in water; (d) EPR signals of DMPO-•$C_5H_5O_2$ over TB-6 in FAL solution in dark and under light irradiation.

experiments were conducted. As depicted in Fig. S8, the rate of H_2O_2 formation on TB-6 is greatly inhibited when O_2 is replaced by air or N_2. Therefore, O_2 reduction is the dominating process for H_2O_2 formation. As shown in Fig. 7a, the H_2O_2 yield significantly drops in the absence of FAL because the photogenerated holes cannot be efficiently consumed, leading to hole accumulation and faster electron–hole recombination. Furthermore, the yield slightly decreases when TEOA (h$^+$ scavenger) or IPA (•OH scavenger) is added, implying that h$^+$ and •OH are not the main active species for photocatalytic H_2O_2 evolution. It excludes the possibility of H_2O_2 formation from water oxidation (2 H_2O + 2 h$^+$ → H_2O_2 + 2 H$^+$) [51,52]. Instead, H_2O_2 production is greatly inhibited by adding AgNO$_3$ (e$^-$ scavenger) and p-benzoquinone (BQ, •O_2^- scavenger), indicating that H_2O_2 originates from O_2 reduction by e$^-$ with •O_2^- as the intermediates [53,54].

To detect the active species and intermediates during O_2 reduction and FAL oxidation on TB-6, electron paramagnetic resonance (EPR) measurements were taken using DMPO as the radical trapping agent [55–59]. All samples exhibit DMPO-•O_2^- signals in O_2-saturated methanol under light irradiation (Fig. 7b), since their CB positions are all higher than the electrode potential of O_2/•O_2^- (−0.33 V vs NHE) [60]. The strongest signal is observed on TB-6, indicating its strongest reducing power. Also, the results suggest that H_2O_2 is formed by a sequential two-step O_2 reduction reaction. In addition, the strongest DMPO-•OH signal is detected for TB-6 (Fig. 7c), indicating that the photogenerated holes in TiO$_2$ VB are used for •OH production instead those in BTTA HOMO, since BTTA shows negligible •OH signal. The EPR measurements suggest that the photogenerated charge carriers with

higher redox power are retained for reactions, demonstrating the superiority of S-scheme heterojunction. Subsequently, •$C_5H_5O_2$ radicals in FAL solutions under light illumination was detected. As shown in Fig. 7d, the characteristic sixfold peaks correlate to the DMPO–Cα radical (•$C_5H_5O_2$), which is resulted from the selective activation of the Cα–H bond of FAL [61]. The hydrogen atom bound to α-C reacts with a photogenerated hole to form a proton and a •$C_5H_5O_2$ radical [62]. The signal grows under prolonged illumination, confirming that •$C_5H_5O_2$ is the crucial intermediate during selective FAL oxidation.

In-situ diffuse reflectance infrared Fourier transform spectroscopy (DRIFTS) measurements were conducted to monitor surface adsorbed species and reaction intermediates. When TB-6 is exposed to a vapor mixture of FAL, H_2O, and O_2 in dark for 1 h, the absorption peaks of FAL and H_2O emerge, and their intensities gradually increase. In Fig. 8a, two peaks are observed at 1501 and 1155 cm^{-1}, assigned to the C=C and C–O–C stretching of the furan rings [63]. Meanwhile, the peak at 1454 cm^{-1} could be attributed to the CH$_2$ bending of FAL, and the peak at 3270 cm^{-1} is attributed to the O–H bond of FAL. In addition, two new peaks at 1650 and 3368 cm^{-1} are assigned to the deformation vibration of H_2O molecules. With light on (0–60 min), the absorption peaks of O–H bond of FAL and H_2O diminish due to the consumption of FAL and H_2O (Fig. 8b). Simultaneously, two new peaks appear at 1740 and 1548 cm^{-1}, corresponding to the stretching of C=O and COOH [64]. These two peaks strengthen over time due to the generation of FF and FAC. Also, another gradually increasing peak at ~1070 cm^{-1} is assigned to OOH* , which is formed during the protonation of a •O_2^- radical. The OOH* can be further reduced by an electron to generate H_2O_2.
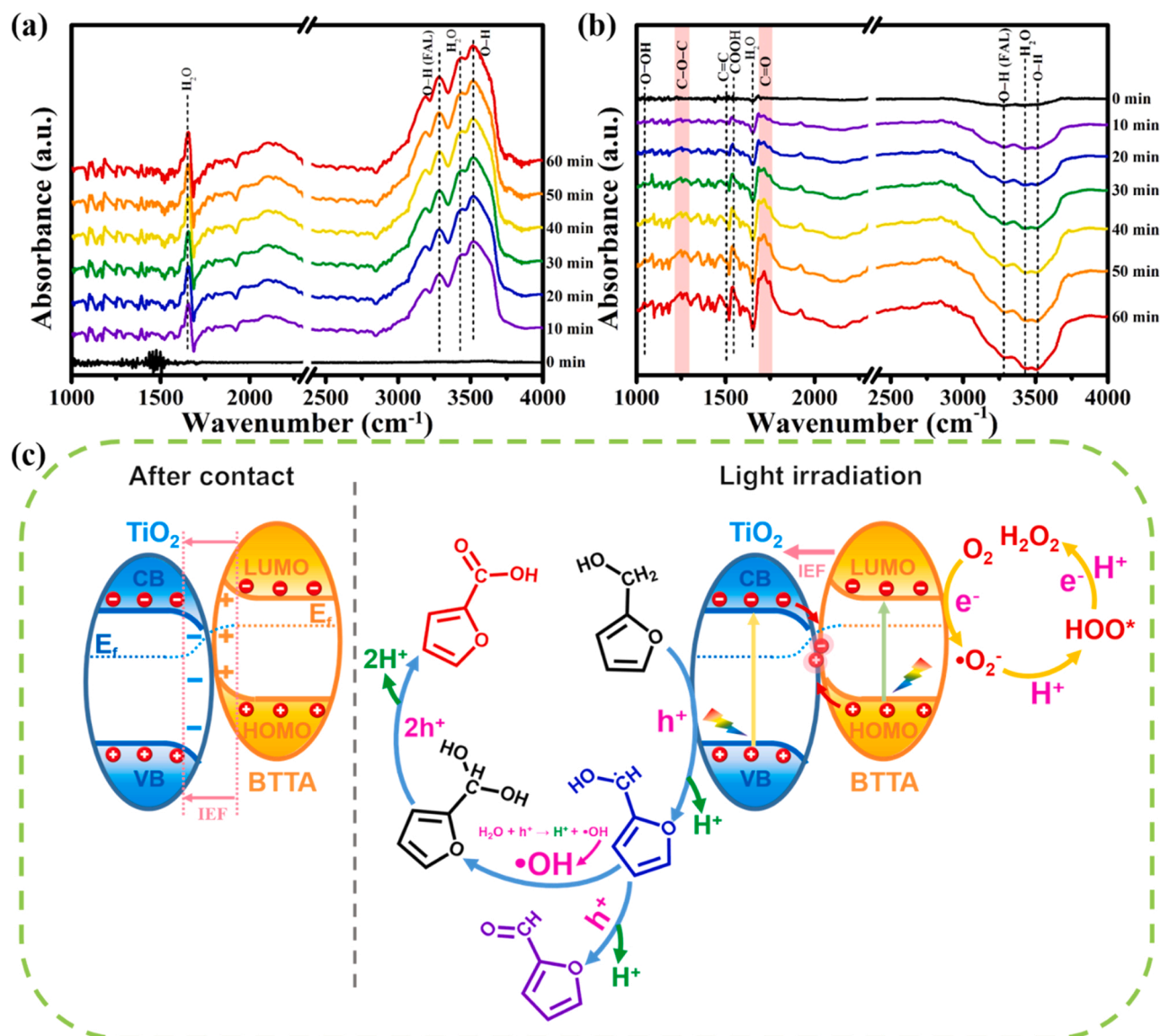
Fig. 8. In-situ DRIFTS spectra of TB-6 under the exposure of H_2O, FAL, and O_2 (a) in dark and (b) under light irradiation ($\lambda = 365$ nm); (c) Proposed reaction pathway of photocatalytic FAL oxidation coupled with H_2O_2 production.

Based on the results above, the overall reaction mechanism is proposed (Fig. 8c). First, light irradiation over TB-6 generates electron–hole pairs. Following the S-scheme mechanism, the useful photogenerated electrons and holes are reserved in the LUMO of BTTA and the VB of TiO_2, respectively. On the one hand, the electrons are used to reduce O_2 to $\bullet O_2^-$, which is further reduced to H_2O_2. On the other hand, the holes activate the α-C–H bond of FAL to generate $\bullet C_5H_5O_2$ radicals and protons. The $\bullet C_5H_5O_2$ undergoes further oxidation via two different pathways. Frist, the h^+ oxidize $\bullet C_5H_5O_2$ to FF, during which the hydrogen atoms in the hydroxyl groups of $\bullet C_5H_5O_2$ are snatched away. Second, the h^+ can also react with H_2O to form $\bullet OH$, which reacts with $\bullet C_5H_5O_2$ to form a diol intermediate. The unstable diol is ultimately converted into FAC after dehydrogenation.

4. Conclusions

In summary, S-scheme TiO_2 @BTTA photocatalysts were successfully prepared by encapsulating TiO_2 NFs with the BTTA COF. The TiO_2 @BTTA composites own the advantages of large specific surface areas, good light absorption performance, and high carrier separation efficiency. Moreover, the S-scheme heterojunction efficiently facilitates carrier separation and enhances redox power. The TB-6 composite shows the highest activity of H_2O_2 production coupled with FAL oxidation. The conversion of FAL is nearly 92 %, and the H_2O_2-evolution rate reaches 740 μmol L^{-1} h^{-1}. Mechanistic studies show that H_2O_2 is formed through the two-step single-electron O_2 reduction. Meanwhile, FAL is activated to $\bullet C_5H_5O_2$ by h^+ and is further oxidized to FF or FAC by reacting with h^+ or $\bullet OH$, respectively This study not only presents a rational design of S-scheme photocatalysts by in-situ growing COFs on the surface of inorganic photocatalysts, but also shows the efficient utilization of photogenerated charge carriers by coupling H_2O_2 production with FAL oxidation.

CRediT authorship contribution statement

Yi Yang: Methodology, Data curation, Writing – original draft. **Jingjing Liu:** Investigation. **Miaoli Gu:** Investigation, Resources. **Bei Cheng:** Investigation, Funding acquisition. **Linxi Wang:** Conceptualization, Supervision, Funding acquisition, Writing – review & editing. **Jiaguo Yu:** Project administration, Supervision, Funding acquisition.

Declaration of Competing Interest

Data availability

Data will be made available on request.

Acknowledgements

Appendix A. Supporting information

Supplementary data associated with this article can be found in the online version at doi:10.1016/j.apcatb.2023.122780.

References

[1] L. Wang, J. Zhang, Y. Zhang, H. Yu, Y. Qu, J. Yu, Inorganic metal-oxide photocatalyst for H_2O_2 production, Small 18 (2022), 2104561.

[2] H. Hirakawa, S. Shiota, Y. Shiraishi, S. Sakamoto, S. Ichikawa, T. Hirai, Au nanoparticles supported on $BiVO_4$: effective inorganic photocatalysts for H_2O_2 production from water and O_2 under visible light, ACS Catal. 6 (2016) 4976–4982.

[3] R. He, D. Xu, X. Li, Floatable S-scheme photocatalyst for H_2O_2 production and organic synthesis, J. Mater. Sci. Technol. 138 (2023) 256–258.

[4] H. Che, X. Gao, J. Chen, J. Hou, Y. Ao, P. Wang, Iodide-induced fragmentation of polymerized hydrophilic carbon nitride for high-performance quasi-homogeneous photocatalytic H_2O_2 production, Angew. Chem. Int. Ed. 60 (2021) 25546–25550.

[5] Z. Wang, Y. Zhao, Y. Zhou, X. Wang, H. Huang, Y. Liu, M. Shao, Z. Kang, All-in-one photocatalysis device for one-step high concentration H_2O_2 photoproduction, Chem. Eng. J. 427 (2022), 131972.

[6] L. Liu, M.Y. Gao, H. Yang, X. Wang, X. Li, A.I. Cooper, Linear conjugated polymers for solar-driven hydrogen peroxide production: the importance of catalyst stability, J. Am. Chem. Soc. 143 (2021) 19287–19293.

[7] F. Xue, Y. Si, M. Wang, M. Liu, L. Guo, Toward efficient photocatalytic pure water splitting for simultaneous H_2 and H_2O_2 production, Nano Energy 62 (2019) 823–831.

[8] Y. Yang, Z. Zeng, G. Zeng, D. Huang, R. Xiao, C. Zhang, C. Zhou, W. Xiong, W. Wang, M. Cheng, W. Xue, H. Guo, X. Tang, D. He, Ti_3C_2 Mxene/porous g-C_3N_4 interfacial Schottky junction for boosting spatial charge separation in photocatalytic H_2O_2 production, Appl. Catal. B Environ. 258 (2019) 117956.

[9] G. Han, F. Xu, B. Cheng, Y. Li, J. Yu, L. Zhang, Enhanced photocatalytic H_2O_2 production over inverse opal ZnO@polydopamine S-scheme heterojunctions, Acta Phys. Chim. Sin. 38 (2022) 2112037.

[10] Y. Kofuji, S. Ohkita, Y. Shiraishi, H. Sakamoto, S. Tanaka, S. Ichikawa, T. Hirai, Graphitic carbon nitride doped with biphenyl diimide: efficient photocatalyst for hydrogen peroxide production from water and molecular oxygen by sunlight, ACS Catal. 6 (2016) 7021–7029.

[11] G. Han, Y.H. Jin, R.A. Burgess, N.E. Dickenson, X.M. Cao, Y. Sun, Visible-light-driven valorization of biomass intermediates integrated with H_2 production catalyzed by ultrathin Ni/CdS nanosheets, J. Am. Chem. Soc. 139 (2017) 15584–15587.

[12] Z. Wang, L. Wang, B. Cheng, H. Yu, J. Yu, Photocatalytic H_2 evolution coupled with furfuralcohol oxidation over Pt-modified ZnCdS solid solution, Small Methods 5 (2021), 2100979.

[13] B. He, Z. Wang, P. Xiao, T. Chen, J. Yu, L. Zhang, Cooperative coupling of H_2O_2 production and organic synthesis over a floatable polystyrene-sphere-supported TiO_2/Bi_2O_3 S-scheme photocatalyst, Adv. Mater. 34 (2022), 2203225.

[14] M. Tahir, B. Tahir, Constructing S-scheme 2D/0D g-C_3N_4/TiO_2 NPs/MPs heterojunction with 2D-Ti_3AlC_2 MAX cocatalyst for photocatalytic CO_2 reduction to CO/CH_4 in fixed-bed and monolith photoreactors, J. Mater. Sci. Technol. 106 (2022) 195–210.

[15] G. Alnaggar, K. Alkanad, S.S.G. Chandrashekar, M.A. Bajiri, Q.A. Drmosh, L. N. Krishnappagowda, S. Ananda, Rational design of a 2D TiO_2–MoO_3 step-scheme heterostructure for boosted photocatalytic overall water splitting, New J. Chem. 46 (2022) 9629–9640.

[16] Y. Hong, Y. Cho, E.M. Go, P. Sharma, H. Cho, B. Lee, S.M. Lee, S.O. Park, M. Ko, S. K. Kwak, C. Yang, J.-W. Jang, Unassisted photocatalytic H_2O_2 production under visible light by fluorinated polymer-TiO_2 heterojunction, Chem. Eng. J. 418 (2021), 129346.

[17] G. Zhang, D. Chen, N. Li, Q. Xu, H. Li, J. He, J. Lu, Fabrication of Bi_2MoO_6/ZnO hierarchical heterostructures with enhanced visible-light photocatalytic activity, Appl. Catal. B Environ. 250 (2019) 313–324.

[18] Y. Yang, J. Wu, B. Cheng, L. Zhang, A.A. Al-Ghamdi, S. Wageh, Y. Li, Enhanced photocatalytic H_2-production activity of CdS nanoflower using single atom Pt and graphene quantum dot as dual cocatalysts, Chin. J. Struct. Chem. 41 (2022) 6–23.

[19] J.H. Lee, H. Cho, S.O. Park, J.M. Hwang, Y. Hong, P. Sharma, W.C. Jeon, Y. Cho, C. Yang, S.K. Kwak, H.R. Moon, J.-W. Jang, High performance H_2O_2 production achieved by sulfur-doped carbon on CdS photocatalyst via inhibiting reverse H_2O_2 decomposition, Appl. Catal. B Environ. 284 (2021), 119690.

[20] X. Zhang, J. Yu, W. Macyk, S. Wageh, A.A. Al-Ghamdi, L. Wang, C_3N_4/PDA S-scheme heterojunction with enhanced photocatalytic H_2O_2 production performance and its mechanism, Adv. Sustain. Syst. 7 (2023), 2200113.

[21] Y. Li, Z. Xia, Q. Yang, L. Wang, Y. Xing, Review on g-C_3N_4-based S-scheme heterojunction photocatalysts, J. Mater. Sci. Technol. 125 (2022) 128–144.

[22] W. Wang, H. Zhang, Y. Chen, H. Shi, Efficient degradation of tetracycline via coupling of photocatalysis and photo-Fenton processes over a 2D/2D α-Fe_2O_3/g-C_3N_4 S-scheme heterojunction catalyst, Acta Phys. Chim. Sin. 38 (2022), 2201008.

[23] A. Ali Khan, M. Tahir, Constructing S-scheme heterojunction of CoAlLa-LDH/g-C_3N_4 through monolayer Ti_3C_2-MXene to promote photocatalytic CO_2 reforming of methane to solar fuels, ACS Appl. Energy Mater. 5 (2022) 784–806.

[24] Z. Jiang, B. Cheng, Y. Zhang, S. Wageh, A.A. Al-Ghamdi, J. Yu, L. Wang, S-scheme ZnO/WO_3 heterojunction photocatalyst for efficient H_2O_2 production, J. Mater. Sci. Technol. 124 (2022) 193–201.

[25] A. Meng, S. Zhou, D. Wen, P. Han, Y. Su, g-C_3N_4/$CoTiO_3$ S-scheme heterojunction for enhanced visible light hydrogen production through photocatalytic pure water splitting, Chin. J. Catal. 43 (2022) 2548–2557.

[26] Y. Zhu, Y. Zhuang, L. Wang, H. Tang, X. Meng, X. She, Constructing 0D/1D Ag_3PO_4/TiO_2 S-scheme heterojunction for efficient photodegradation and oxygen evolution, Chin. J. Catal. 43 (2022) 2558–2568.

[27] L. Wang, J. Zhang, H. Yu, I.H. Patir, Y. Li, S. Wageh, A.A. Al-Ghamdi, J. Yu, Dynamics of photogenerated charge carriers in inorganic/organic S-scheme heterojunctions, J. Phys. Chem. Lett. 13 (2022) 4695–4700.

[28] K. Saravanakumar, V. Maheskumar, Y. Yea, Y. Yoon, V. Muthuraj, C.M. Park, 2D/2D nitrogen-rich graphitic carbon nitride coupled Bi_2WO_6 S-scheme heterojunction for boosting photodegradation of tetracycline: Influencing factors, intermediates, and insights into the mechanism, Compos. Part B 234 (2022), 109726.

[29] Y. Yang, B. Cheng, J. Yu, L. Wang, W. Ho, TiO_2/In_2S_3 S-scheme photocatalyst with enhanced H_2O_2-production activity, Nano Res. 16 (2023) 4506–4514.

[30] Y. Yang, B. Zhu, L. Wang, B. Cheng, L. Zhang, J. Yu, In-situ grown N, S co-doped graphene on TiO_2 fiber for artificial photosynthesis of H_2O_2 and mechanism study, Appl. Catal. B Environ. 317 (2022), 121788.

[31] C. Kang, Z. Zhang, V. Wee, A.K. Usadi, D.C. Calabro, L.S. Baugh, S. Wang, Y. Wang, D. Zhao, Interlayer shifting in two-dimensional covalent organic frameworks, J. Am. Chem. Soc. 142 (2020) 12995–13002.

[32] Y. Wang, Q. Yang, F. Yi, R. Lu, Y. Chen, C. Liu, X. Li, C. Wang, H. Yan, NH_2-UiO-66 coated with two-dimensional covalent organic frameworks: High stability and photocatalytic activity, ACS Appl. Mater. Interfaces 13 (2021) 29916–29925.

[33] Y. Zhang, J. Qiu, B. Zhu, M.V. Fedin, B. Cheng, J. Yu, L. Zhang, ZnO/COF S-scheme heterojunction for improved photocatalytic H_2O_2 production performance, Chem. Eng. J. 444 (2022) 136584.

[34] J.L. Shi, R. Chen, H. Hao, C. Wang, X. Lang, 2D sp^2 carbon-conjugated porphyrin covalent organic framework for cooperative photocatalysis with TEMPO, Angew. Chem. Int. Ed. 59 (2020) 9088–9093.

[35] Y. Deng, Z. Peng, D. Du, X. Ning, Y. Wang, D. Zhang, J. Liu, S. Zhang, X. Lu, Embedding ultrasmall Au clusters into the pores of a covalent organic framework for enhanced photostability and photocatalytic performance, Angew. Chem. Int. Ed. 59 (2020) 6082–6089.

[36] W. Chen, L. Wang, D. Mo, F. He, Z. Wen, X. Wu, H. Xu, L. Chen, Modulating benzothiadiazole-based covalent organic frameworks via halogenation for enhanced photocatalytic water splitting, Angew. Chem. Int. Ed. 59 (2020) 16902–16909.

[37] L. Liu, J. Zhang, X. Tan, B. Zhang, J. Shi, X. Cheng, D. Tan, B. Han, L. Zheng, F. Zhang, Supercritical CO_2 produces the visible-light-responsive TiO_2/COF heterojunction with enhanced electron-hole separation for high-performance hydrogen evolution, Nano Res. 13 (2020) 983–988.

[38] S. Kang, J. Hwang, rGO-wrapped Ag-doped TiO_2 nanofibers for photocatalytic CO_2 reduction under visible light, J. Clean. Prod. 374 (2022), 134022.

[39] P. Dong, Y. Wang, A. Zhang, T. Cheng, X. Xi, J. Zhang, Platinum single atoms anchored on a covalent organic framework: boosting active sites for photocatalytic hydrogen evolution, ACS Catal. 11 (2021) 13266–13279.

[40] H. Yu, J. Zhang, X. Yan, C. Wu, X. Zhu, B. Li, T. Li, Q. Guo, J. Gao, M. Hu, J. Yang, Donor–acceptor covalent organic framework hollow submicrospheres with a hierarchical pore structure for visible-light-driven H_2 evolution, J. Mater. Chem. A 10 (2022) 11010–11018.

[41] F.A. Qaraah, S.A. Mahyoub, A. Hezam, A. Qaraah, Q.A. Drmosh, G. Xiu, Construction of 3D flowers-like O-doped g-C_3N_4-[N-doped Nb_2O_5/C] heterostructure with direct S-scheme charge transport and highly improved visible-light-driven photocatalytic efficiency, Chin. J. Catal. 43 (2022) 2637–2651.

[42] J. Zhang, L. Zhang, W. Wang, J. Yu, In situ irradiated X-ray photoelectron spectroscopy investigation on electron transfer mechanism in S-scheme photocatalyst, J. Phys. Chem. Lett. 13 (2022) 8462–8469.

[43] A. Shawky, R.M. Mohamed, S-scheme heterojunctions: Emerging designed photocatalysts toward green energy and environmental remediation redox reactions, J. Environ. Chem. Eng. 10 (2022), 108249.

[44] K. Xu, J. Shen, S. Zhang, D. Xu, X. Chen, Efficient interfacial charge transfer of $BiOCl$-In_2O_3 step-scheme heterojunction for boosted photocatalytic degradation of ciprofloxacin, J. Mater. Sci. Technol. 121 (2022) 236–244.

[45] K.K. Das, S. Mansingh, D.P. Sahoo, R. Mohanty, K. Parida, Engineering an oxygen-vacancy-mediated step-scheme charge carrier dynamic coupling $WO_{3-x}/ZnFe_2O_4$ heterojunction for robust photo-Fenton-driven levofloxacin detoxification, New J. Chem. 46 (2022) 5785–5798.

[46] L. Wang, C. Bie, J. Yu, Challenges of Z-scheme photocatalytic mechanisms, Trends Chem. 4 (2022) 973–983.

[47] V.-H. Nguyen, P. Singh, A. Sudhaik, P. Raizada, Q.V. Le, E.T. Helmy, Novel step-scheme (S-scheme) heterojunction photocatalysts toward artificial photosynthesis, Mater. Lett. 313 (2022), 131781.

[48] Q. Xu, S. Wageh, A.A. Al-Ghamdi, X. Li, Design principle of S-scheme heterojunction photocatalyst, J. Mater. Sci. Technol. 124 (2022) 171–173.

[49] M. Gu, Y. Yang, L. Zhang, B. Zhu, G. Liang, J. Yu, Efficient sacrificial-agent-free solar H_2O_2 production over all-inorganic S-scheme composites, Appl. Catal. B Environ. 324 (2023), 122227.

[50] R. Gao, J. Bai, R. Shen, L. Hao, C. Huang, L. Wang, G. Liang, P. Zhang, X. Li, 2D/2D covalent organic framework/CdS Z-scheme heterojunction for enhanced photocatalytic H_2 evolution: Insights into interfacial charge transfer mechanism, J. Mater. Sci. Technol. 137 (2023) 223–231.

[51] B. Liu, C. Bie, Y. Zhang, L. Wang, Y. Li, J. Yu, Hierarchically porous ZnO/g-C_3N_4 S-scheme heterojunction photocatalyst for efficient H_2O_2 production, Langmuir 37 (2021) 14114–14124.

[52] L. Wang, T. Yang, L. Peng, Q. Zhang, X. She, H. Tang, Q. Liu, Dual transfer channels of photo-carriers in 2D/2D/2D sandwich-like $ZnIn_2S_4$/g-C_3N_4/Ti_3C_2 MXene S-scheme/Schottky heterojunction for boosting photocatalytic H_2 evolution, Chin. J. Catal. 43 (2022) 2720–2731.

[53] Y. Wang, D. Meng, X. Zhao, Visible-light-driven H_2O_2 production from O_2 reduction with nitrogen vacancy-rich and porous graphitic carbon nitride, Appl. Catal. B Environ. 273 (2020) 119064.

[54] X. Zhao, Y. You, S. Huang, Y. Wu, Y. Ma, G. Zhang, Z. Zhang, Z-scheme photocatalytic production of hydrogen peroxide over $Bi_4O_5Br_2$/g-C_3N_4 heterostructure under visible light, Appl. Catal. B Environ. 278 (2020) 119251.

[55] Z. Jiang, Y. Zhang, L. Zhang, B. Cheng, L. Wang, Effect of calcination temperatures on photocatalytic H_2O_2-production activity of ZnO nanorods, Chin. J. Catal. 43 (2022) 226–233.

[56] L. Zhou, Y. Li, Y. Zhang, L. Qiu, Y. Xing, A 0D/2D $Bi_4V_2O_{11}$/g-C_3N_4 S-scheme heterojunction with rapid interfacial charges migration for photocatalytic antibiotic degradation, Acta Phys. Chim. Sin. 38 (2022), 2112027.

[57] P. Shandilya, A. Guleria, B. Fang, A magnetically recyclable dual step-scheme $Bi_2WO_6/Fe_2O_3/WO_3$ heterojunction for photodegradation of bisphenol-A from aqueous solution, J. Environ. Chem. Eng. 9 (2021), 106461.

[58] Y. Lu, X. Jia, Z. Ma, Y. Li, S. Yue, X. Liu, J. Zhang, W^{-5+}–W^{5+} pair induced LSPR of $W_{18}O_{49}$ to sensitize $ZnIn_2S_4$ for full-spectrum solar-light-driven photocatalytic hydrogen evolution, Adv. Funct. Mater. 32 (2022), 2203638.

[59] J. Wu, B. Ding, X. Qian, L. Mao, H. Zheng, L. Zhang, S. Zheng, J. Zhang, Nanosheets loaded on tetrahedral surfaces form a Z-type Bi_2MoO_6/γ-Bi_2O_3 heterojunction to enhance the photocatalytic degradation activity of lomefloxacin and Rhodamine B, Dalton Trans. 51 (2022) 15797–15805.

[60] J. Zhao, M. Ji, H. Chen, Y.-X. Weng, J. Zhong, Y. Li, S. Wang, Z. Chen, J. Xia, H. Li, Interfacial chemical bond modulated $Bi_{19}S_{27}Br_3$/g-C_3N_4 Z-scheme heterojunction for enhanced photocatalytic CO_2 conversion, Appl. Catal. B Environ. 307 (2022), 121162.

[61] C.-L. Tan, M.-Y. Qi, Z.-R. Tang, Y.-J. Xu, Cocatalyst decorated $ZnIn_2S_4$ composites for cooperative alcohol conversion and H_2 evolution, Appl. Catal. B Environ. 298 (2021), 120541.

[62] S. Hameed, L. Lin, A. Wang, W. Luo, Recent developments in metal-based catalysts for the catalytic aerobic oxidation of 5-hydroxymethyl-furfural to 2,5-furandicarboxylic acid, Catalysts 10 (2020) 120.

[63] H. Wang, Y. Song, J. Xiong, J. Bi, L. Li, Y. Yu, S. Liang, L. Wu, Highly selective oxidation of furfuryl alcohol over monolayer titanate nanosheet under visible light irradiation, Appl. Catal. B Environ. 224 (2018) 394–403.

[64] B. Wang, W. Zhang, G. Liu, H. Chen, Y.X. Weng, H. Li, P.K. Chu, J. Xia, Excited electron-rich $Bi^{(3-x)+}$ sites: A quantum well-like structure for highly promoted selective photocatalytic CO_2 reduction performance, Adv. Funct. Mater. 32 (2022), 2202885.